

pubs.acs.org/JPCC Article

Plasmon-Induced Hot-Carrier Excited-State Dynamics in Plasmonic Semiconductor Nanocrystals

Jason E. Kuszynski, Catherine J. Fabiano, Edward T. Nguyen, Keyou Mao, Anoushka K. Ahuja, Richard D. Schaller,* and Geoffrey F. Strouse*



Cite This: J. Phys. Chem. C 2023, 127, 22654-22661



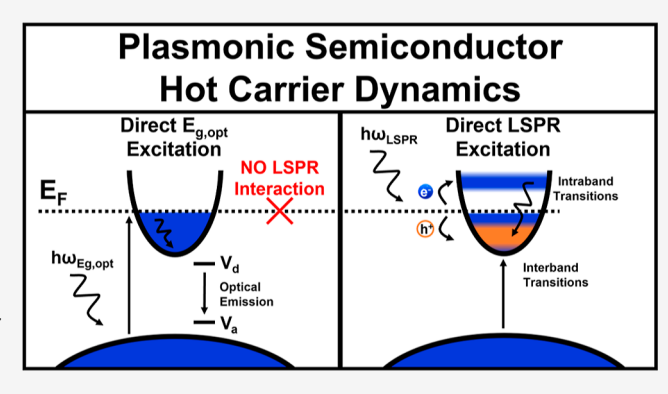
ACCESS I

III Metrics & More

Article Recommendations

Supporting Information

ABSTRACT: The variance of carrier relaxation pathways for WO_{3-x} plasmonic semiconductor nanocrystals (PSNCs) is monitored by transient absorption spectroscopy following excitation of the localized surface plasmon resonance (LSPR) versus the optical band gap ($E_{\rm g,opt}$). Excitation of the LSPR leads to efficient hot carrier population above the Fermi level in WO_{3-x} via Landau damping, in analogy to noble metal LSPR relaxation mechanisms. Hot carrier depopulation occurs on the femtosecond timescale, observed as the concomitant recovery of an LSPR bleach with the appearance of discrete interband and intraband photoinduced absorption features. By comparison, the direct excitation of $E_{\rm g,opt}$ results in trion recombination at donor—acceptor sites within the WO_{3-x} NC, consistent with exciton decay dynamics observed



for typical wide-band-gap semiconductor NCs. From the analysis of pump power dependency data, a hot-carrier electron—phonon coupling constant of 1.47×10^{11} J K⁻¹ s⁻¹ cm⁻³ is extracted. The direct comparison of the decay dynamics following $E_{\rm g,opt}$ versus LSPR excitation confirms that the observed plasmon in trioctylphosphine oxide passivated, spherical WO_{3-x} is a resonance state in which hot carriers are generated only from excitation on resonance with the LSPR frequency. This study on WO_{3-x} PSNCs provides a toolset that can be used to evaluate the role of hot carriers following LSPR excitation of n-type, plasmonic transparent conducting oxide NCs, where enhancement of photocatalysis, photovoltaic performance, and optical enhancement has been reported.

■ INTRODUCTION

A goal in plasmonic materials research is the coupling of plasmonic, electronic, and photonic properties in materials at the nanoscale to enhance device performance. In noble metal and wide-band-gap plasmonic semiconductor nanocrystals (PSNCs), excitation into the localized surface plasmon resonance (LSPR) is observed to enhance catalytic properties at the NC surface.^{2,3} While noble metal NC photocatalysts are common in the literature, the use of PSNCs would be advantageous due to their lower costs, high carrier concentrations, ease of plasmon frequency tunability, and lack of visible-light absorption.^{4–9} In general, the LSPR in wide-band-gap metal oxides is attributed to oxygen vacancies (V_O), resulting in a highly tunable plasmon frequency.¹⁰ Despite discrepancies, there is considerable agreement that a collection of mobile charge carriers (free or constrained, plasmonic, ^{2,11,12} or polaronic ^{13–15}) is responsible for the extinction feature in question and its subsequent material enhancement capabilities. The role of LSPR excitation on catalyst improvement has been attributed to near-field enhancement, hot carrier formation at the NC surface, and carrier trapping at surface-bound donor sites. Hot carriers were observed experimentally and reported to occur through

Landau damping by electron—electron scattering in the Fermi sea of electrons. Whether hot carriers are formed following LSPR excitation in metal oxide PSNCs is not fully evaluated as the presence of surface trap sites may play a pivotal role in LSPR relaxation pathways. The role of hot carriers versus surface trap sites in wide-band-gap metal oxide PSNCs can be evaluated by direct comparison of the dynamics for plasmon relaxation following excitation of the LSPR versus the optical band gap ($E_{\rm g,opt}$). The hot-carrier relaxation dynamics can be directly probed using femtosecond transient absorption (fsTA) to observe simultaneous ground-state bleaching of the plasmon, along with relaxation through the semiconducting electronic structure of the metal oxide.

In this article, the relaxation dynamics leading to the formation of hot carriers following excitation of the LSPR of trioctylphosphine oxide (TOPO) passivated, spherical WO_{3-x}

Received: August 1, 2023
Revised: September 23, 2023
Published: November 8, 2023





 $(2.4 \pm 0.3 \text{ nm})$ are evaluated through TA. The WO_{3-x} nanoparticles have a plasmon extinction feature centered at 1.65 eV with Drude calculated carrier densities of 2×10^{21} ${\rm cm}^{-3}$. Carrier densities are validated with chemical titration and fitting to Drude model analyses. ^{19–21} Upon directly exciting the LSPR in WO_{3-x}, hot carrier relaxation originating from <100 fs Landau damping is observed in the TA spectra as spectrally distinct populations of interband and intraband transitions concomitant with the recovery of the LSPR. On the contrary, when $E_{\rm g,opt}$ is excited, donor-acceptor $({
m V_d-V_a})$ trion recombination is experimentally observed. The experimental data support a model where plasmon relaxation in PSNCs generates hot carriers through Landau damping, followed by relaxation through the electronic structure of the PSNC. The lack of interband and intraband absorptions when $E_{\rm g,opt}$ is directly excited further supports the idea that the LSPR is a resonant state that is not directly coupled to the band structure of the PSNC, consistent with observations in noble metal NCs. To date, exploration of hot carrier formation in wide-band-gap plasmonic metal oxides (F,In:CdO; WO_{3-x}) has only recently been explored using indirect measures, including fs electron transfer to a dye as an indirect probe of the presence of hot carriers or intraband relaxation for the ptype case $(Cu_{2-r}S/Se)$. The full UV-vis-NIR hot carrier spectra are typically not reported in the literature for n-type metal oxide plasmonic semiconductors, and they have instead focused on individual features in the spectra. To the authors' knowledge, there has been no complete fs UV-vis-NIR spectral analysis of hot carrier relaxation pathways in a PSNC thus far. The confirmation of hot carriers in WO_{3-x} that behave analogously to noble metals would allow the implementation of cheaper and more controllable materials for applications where hot carriers can enhance the efficiency of photovoltaic, photocatalytic, optoelectronic, and thermoelectric technologies. 22-26

METHODS

Materials. Tungsten(IV)chloride (WCl₄, 95%), nitrosyl tetrafluoroborate (NOBF₄, 95%), and toluene (\geq 99.5%) were purchased from Sigma-Aldrich. TOPO (98%) was obtained from Alfa Aesar. Oleic acid (OA, technical grade, 90%) and acetonitrile (MeCN) were obtained from VWR.

Microwave Synthesis. In a 10 mL microwave vial (CEM), 30 mg (92.1 μ mol) of WCl₄ and 400 μ L (1.27 mmol) of OA were combined and transferred for reaction in a microwave reactor (CEM). After insertion, the precursors underwent constant microwave irradiation at 300 W with the vial uncapped for 5 min. After the reaction was complete, vials were immediately removed and quenched with toluene, and the resulting NC suspension was transferred to a gel permeation chromatography column to clean and remove excess ligands. After cleaning, 1 mg of TOPO was added to the WO_{2.76} suspension and heated to 65 °C while stirring to ligand exchange the native OA for TOPO to improve stability.

Extinction Spectroscopy. WO $_{2.76}$ NCs were suspended in toluene and diluted until a LSPR of between 0.8-1.0 absorbance units was obtained under an inert (N_2) atmosphere. The suspension was prepared in a 1 mm spectrophotometer cell (Starna Cells, Inc.) on a Varian Cary Bio 50 UV-vis spectrophotometer. A baseline correction was performed with neat toluene.

PL with PL Excitation (PLE). WO_{2.76} NCs were prepared similarly to the methods used for extinction spectroscopy. The

suspension was prepared in a submicro fluorometer cell (Starna Cells, Inc.) where PL and PLE spectra were collected on a Varian Cary Eclipse fluorescence spectrophotometer.

Chemical Titration. After preparation and weighing of pristine TOPO-WO_{3-x}, the samples were dissolved in dry toluene in an inert atmosphere glovebox. A known concentration of NOBF₄ dissolved in MeCN was titrated into the NC suspension and left to react for 30 min. The LSPR of the oxidized sample was then measured by the same instrument as described in the Extinction Spectroscopy Section above. This procedure was repeated until the LSPR showed no decrease in extinction after oxidation.

pXRD. X-ray powder patterns were collected at room temperature on a Rigaku Miniflex powder diffractometer (Cu K\$\alpha\$ source). Samples were dried out, ground to a fine powder, and loaded onto a zero-background micropowder plate. Scans were collected from 10 to 80° 2\$\theta\$ at a rate of 5°/min and a 0.1° step size. The whole pattern fitting was completed using Rigaku SmartLab Studio software.

HRTEM. Size, size dispersity, morphology, and lattice fringe analyses were conducted by transmission electron microscopy (TEM). TEM images were collected on a Tecnai Osiris TEM/STEM operating at 200 kV. HR microstructure characterization was performed using an aberration-corrected JEOL ARM 200 F TEM operated at 200 kV. A WO_{3-x} sample was prepared by dispersing the NCs in toluene and octadecylamine (10:1 v/v), heating in an oil bath at 50 °C for 12 h, sonicating in a 40 °C heated bath for 2 min, and running through a gel permeation chromatography column to remove excess ligand and aggregated solid. The solution was drop-cast onto a carbon-coated 200 mesh gold TEM grid (Ted Pella 01840G), excess solvent wicked away with a kimwipe 2 s after deposition, and dried in a vacuum oven at 80 °C for 12 h.

XPS. WO_{3-x} NCs were drop-cast onto a carbon tape in an Ar dry box before transfer into and before insertion into a PHI 5100 X-ray photoelectron spectrometer. X-ray photoelectron spectroscopy (XPS) has an excitation source of Al K α , with a pass energy of 22.36 eV to minimize line width. All samples were calibrated to the aliphatic carbon assignment (C 1s 284.8 eV).

Transient Absorption. Sample preparation for WO_{3-x} NCs was performed using the same methods previously discussed for extinction spectroscopy. fsTA was performed at the center for nanoscale materials (CNMs), where measurements of LSPR and optical band gap pumping were performed. A Ti:sapphire amplifier with a 2 kHz repetition rate and 35 fs pulse width was used, where pump pulses at 325 nm were generated by directing a portion of the 800 nm laser output to an optical parametric amplifier. A small portion of the 800 nm Ti:sapphire output was focused into a sapphire crystal to produce white light probe pulses. Probe pulses were mechanically time-delayed using a translation stage and retroreflector. Also, TA spectra for all time points were averaged over 2 s, and three reproducible separate scans were then averaged together. Background subtraction and probe chirp correction were conducted for all raw spectra before the data analysis. All measurements were performed at room temperature and under ambient conditions. For $E_{\rm g,opt}$ pumped experiments at long time scales (Figure S11, bottom), fsTA measurements were performed at Florida State University (FSU) using a commercial HELIOS Fire instrument with a 1024 pixel CMOS sensor and an expected probe pulse width of

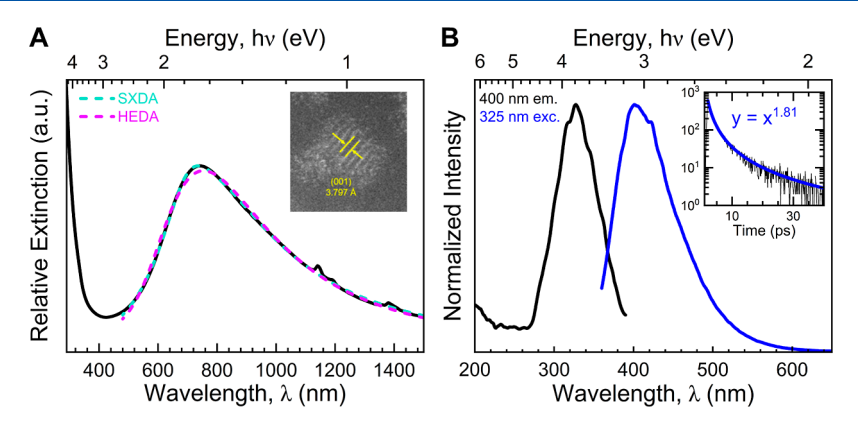


Figure 1. Structural and optical investigation of WO_{2.76}. (A) Extinction spectrum is taken of 2.4 ± 0.3 nm WO_{2.76} where the plasmon frequency is visible at 1.65 eV. The simplified extended Drude approximation (SXDA) along with the heterogeneous extended Drude approximation (HEDA) is fit to the extinction feature, with slightly better agreement from SXDA. HRTEM illustrates a representative WO_{2.76} NC with a (010) lattice spacing of 3.797 Å visible (inset). (B) PL and PLE are performed on the band gap of WO_{2.76} which showcases a 3.80 eV optical band gap and a subsequent emission peak at 3.10 eV with power-law emission dynamics (inset). The emission feature is assigned to a V_0^{2+} to V_0^{0} oxygen defect transition.

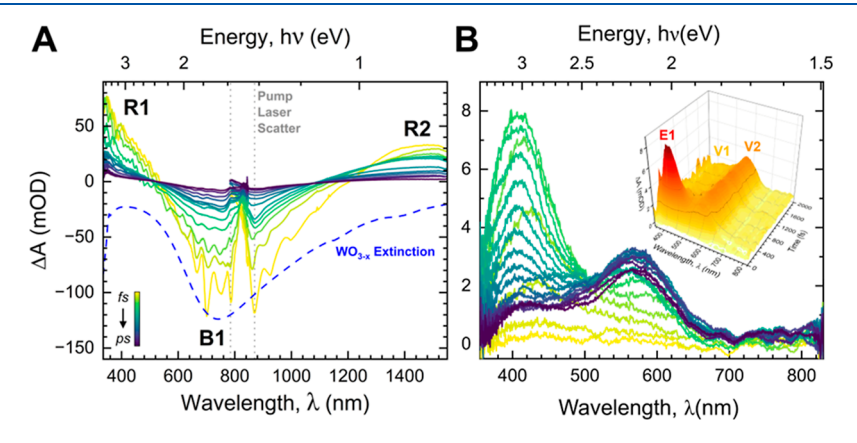


Figure 2. (A) Fs hot carrier equilibration dynamics of WO_{2.76} pumped at 1.65 eV. UV—vis probes and NIR probes are performed to observe hot-carrier relaxation dynamics. Combined, the spectrum reveals dynamics for both hot holes and electrons, where the >3.65 eV PIA, 1.65 eV GSB, and 1.20 eV PIA are attributed to interband transitions of hot electrons to VB, plasmon ground-state bleach, and intraband transitions of hot electrons to hot holes, respectively, as R1, B1, and R2. All features show rapid equilibration of the hot carrier population after Landau damping (<100 fs), leading to dominating electron—phonon and phonon—phonon relaxation pathways. (B) Fs $E_{\rm g,opt}$ dynamics for 3.8 eV pumped WO_{3-x} show three features of interest. (E1) The shortest-lived, high-energy feature at near 3.0 eV is attributed to rapid exciton formation and trion recombination. (V1, V2) Two longer-lived features that slowly grow in between 3.0–2.2 eV are attributed to the excited-state oxygen vacancy population before eventual emission. The inset shows the same data in a 3D plot for easier visualization.

~200 fs with the same averaging, background subtraction, and probe chirp correction methods were used.

RESULTS AND DISCUSSION

Optical and Structural Characterization of WO_{3-x} NCs. TOPO-WO_{3-x} NCs (2.4 \pm 0.3 nm) were prepared by microwave-assisted thermal decomposition of WCl₄ in OA in a 2.45 GHz single mode cavity of a microwave (5 min, 300 W). Synthetic details are provided in the Experimental Section. Size and crystal structure were confirmed by particle distribution and d-spacing analysis. In high-resolution TEM (HRTEM) imaging (Figure 1 and S1), the d-spacing is 3.797 Å and can be assigned to the (010) reflection based on the monoclinic W₁₇O₄₇ crystal structure (P12/m1, ICSD 65084). Confirmation of the crystal structure assignment for WO_{3-x} is provided by comparing the experimental diffractogram to simulated 2 nm WO_{3-x} pXRD patterns (Figure S2 and Table S1). The stoichiometry is assigned as $WO_{2.76}$ (x = 0.24) based on the ratio of the W 4f to the O 2p orbitals in X-ray photoelectron spectra (Figure S3). The plasmon feature for isolated TOPO- $WO_{2.76}$ NCs is stable in air for >40 h with a decay rate for the plasmon extinction of 2.22×10^{-2} h⁻¹ (Figure S4).

In Figure 1A, the extinction spectrum is shown, where the LSPR is observed at 1.65 eV (760 nm) with an optical band gap ($E_{\rm g,opt}$) at 3.80 eV (325 nm). The optical band gap is attained by fitting the optical spectra via a Tauc plot (Figure S5). The carrier density is evaluated by fitting the LSPR feature using the frequency-dependent, SXDA model and compared to the HEDA model, a model that accounts for a distribution of particle sizes.²¹ From the fits, assuming a carrier effective mass of 1.4 m^*/m_e previously reported in the literature, ¹¹ the carrier densities obtained are 2.80×10^{22} (SXDA) and 2.49×10^{22} cm⁻³ (HEDA). The SXDA model provides a slightly better fit than the HEDA model for these samples, likely reflecting the degree of uniformity in the WO_{3-x} samples when prepared via a MW-assisted nucleation synthesis. 28 Since PSNCs can exhibit compensation centers, the carrier density obtained by fitting is compared to chemical titration by NOBF4 as a 1-electron oxidant (Figure S6). The chemical titration yields a value of 1.80×10^{22} cm⁻³, which is in good agreement with the values obtained from SXDA and HEDA modeling, suggesting carrier

compensation is minimal in WO_{3-x} . The observed agreement in carrier density suggests that $NOBF_4$ is an appropriate titrant for WO_{3-x^2} which has been observed to not be the case for $Sn:In_2O_3$. Such an observation may reflect the enhanced stability due to TOPO passivation, removing interfacial compensation centers, as previously suggested by the Milliron and Strouse 19,30 groups as reasons for the lack of agreement between modeling and chemical titrations.

As shown in Figure 1B, the direct excitation of $E_{g,opt}$ (3.80 eV, 325 nm) results in an observed emission at 3.10 eV (400 nm) with an absolute quantum yield of 5%. Excitation of the LSPR (1.65 eV, 750 nm) produces no observable PL. PLE monitored at 3.10 eV yields an absorbing feature at 3.80 eV. The observed emission is assigned to V_0^{2+} donor levels, as has been reported in the literature for other NC tungstates.^{31–34} The V_O²⁺ donor level emission decay is nonexponential but can be fit to a power-law function $(I(x) = Ax^n)$, yielding an exponent (n) of 1.81 (Figure 1B, inset). Power-law behavior for V_O²⁺ emissive centers has been previously reported in defective ZnO and in Cd chalcogenide quantum dots. 35,36 The observation of emission in a plasmonic material is rare but allowable if no electronic interaction or scattering pathway exists to provide nonradiative coupling from the V_O²⁺ donor site to the ground state. Since the experimental measurements are performed on an ensemble, it is not clear if the emission is attributable to a single plasmonic NC possessing both plasmonic behavior and emissive V_0^{2+} donor states or to two separate particles in the ensemble. It is worth noting that pristine WO₃ does not exhibit emission.

Femtosecond Hot Carrier Dynamics of WO_{3-x} NCs. Excitation at 3.80 eV, resonant with the $E_{g,opt}$ or 1.65 eV, resonant with the LSPR, is anticipated to yield discrete optical relaxation behavior. Excitation of $E_{g,opt}$ should lead to exciton recombination via donor—acceptor pair recombination arising at $V_d - V_a$ pairs formed to compensate for V_O sites in $WO_{2.76}$, or recombine with free carriers present in the PSNC, forming a trion (exciton-electron) following Auger processes. The LSPR excitation is anticipated to relax either nonradiatively through scattering processes or through Landau damping, generating hot carriers within the conduction band with subsequent thermalization.

In Figure 2A, resonant excitation of the LSPR at 1.65 eV produces two prominent photoinduced absorption features (R1 and R2) along with a bleach feature (B1). The R1 and R2 absorption features are attributed to the population of electronic levels associated with hot carrier inter- (R1) and intra- (R2) band populations following Landau damping, which generates a nonthermal distribution of the carrier population in the CB.³⁷ The B1 bleach is attributed to the depopulation of the ground-state LSPR extinction. In Table 1, the decay kinetics for the three features are listed for the two

Table 1. LSPR-Pumped (800 nm) Relaxation Rates Obtained at a Fluence of 1.96 mJ/cm² for UV-Vis Probe Lifetimes^a

LSPR pump feature (energy)	electronic relaxation $(au_{ ext{el-ph}}, ext{ fs})$	thermalization $(au_{ ext{ph-ph}}, ext{ps})$
R1 (2.92 eV)	132.2 ± 8.1	3.25 ± 0.44
B1 (1.65 eV)	132.9 ± 2.5	2.39 ± 0.13
R2 (0.84 eV)	198.0 ± 8.4	2.84 ± 1.02

^aFor the NIR probe, R2 is pumped with a fluence of 1.98 mJ/cm².

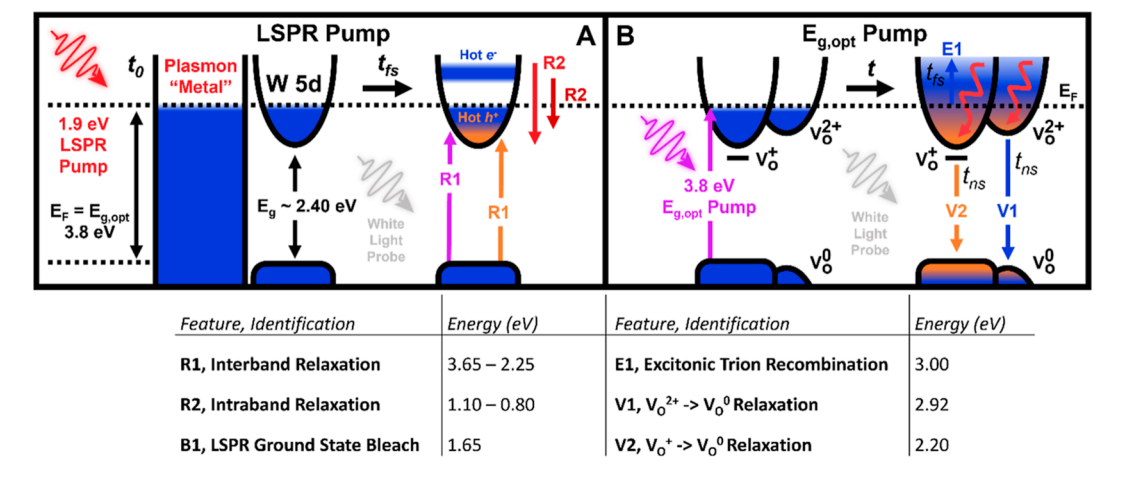
relaxation dynamic regimes. The dynamics of the plasmon bleach (B1) and hot carrier states (R1 and R2) are fit to a biexponential attributed to contributions from electronic relaxation (electron—phonon, el—ph) and thermalization (phonon—phonon mediated energy dissipation, ph—ph) scattering processes, consistent with previous literature of temporal plasmon dynamics. A 3D plot, temporally separated spectral data, and the white light continuum are available in the electronic Supporting Information, Figure S7 and S8.

In Scheme 1, a proposed model delineating the carrier dynamics for WO_{2.76} is shown for selectively exciting the LSPR and $E_{g,opt}$. As shown in Scheme 1A, LSPR pumping results in hot carriers generated through Landau damping subsequently relaxing into interband (R1) and intraband (R2) levels coupled to LSPR (B1). Based on the intersection of R1 and B1 transitions, an electronic band gap of approximately 2.4 eV is assigned based on the 0 ΔA crossing at a long time (4.8 ps), where the lowest energy interband transition is expected to occur during ph-ph relaxation. The maximum is above the limit of the detector (>3.65 eV), limiting the assignment of the R1 energy maximum. The assigned electronic band gap energy is also in relative agreement with previous computational predictions for tungstate systems.³⁹ The boundary between B1 and R2 showcases a maximum interband transition of 1.10 eV, representing the maximum energy difference between the hot holes and electrons, while the smallest energy difference is less than 0.8 eV due to NIR detector limitations. Ultimately, these transition energy ranges support the assertion that the NC electronic band structure plays a critical role in hot-carrier relaxation dynamics in PSNCs.

In Scheme 1B, the excited-state relaxation processes following $E_{\rm g,opt}$ excitation are dominated by exciton recombination events not involving plasmon-induced hot carriers. Combining results from both the PL and fsTA, the fs excitonic feature precedes exciton trapping at $\rm V_d - \rm V_a$ levels arising from the $\rm V_O$ state. The $\rm V_O^{2+}$ (V1) is believed to be associated with the observed power-law type PL, while $\rm V_O^+$ (V2) relaxes nonradiatively.

Pump fluence-dependent transient decay spectra for R1, R2, and B1 pumped on resonance with the LSPR frequency are presented in Figure 3A-C, respectively, while the extracted lifetimes are provided in Table 1 and plotted in Figure S9. Pump fluence is calculated according to the equation, fluence= $\frac{E}{A}$, where $E = \frac{\text{power(W)}}{\text{repetitionrate(Hz)}}$ and A is the beam spot size in cm². Excitation power-dependent TA results indicate only B1 is observed to be strongly fluence-dependent as the rate of bleach recovery for thermalization is known to increase with increasing fluence. 40 B1 features the fastest recombination rates for both el-ph and ph-ph scattering processes, and this correlates with the recovery of the ground-state extinction of the WO_{2.76} LSPR. The feature assigned as R1 has the longest ph-ph lifetime and R2 has the longest el-ph lifetime. The observed bleach, B1, exhibits fluence dependence with an increase in the energy dissipation represented by the ps lifetimes as power increases, while the el-ph lifetime decreases with increasing power. It is hypothesized that the fluencedependent behavior is a result of increased hot carrier production, resulting in an overall decrease in the mean free path for el-ph scattering and thus shortening the lifetime. However, as more energy is dumped into the lattice, ph-ph relaxation is expected to increase due to the increase in the

Scheme 1. (A) Hot Carriers Generated by Plasmon Excitation Relax through the WO_{2.76} Semiconducting Electronic Structure and Observable through R1, R2, and B1^a



"After Landau damping, hot electrons and holes undergo various relaxation processes and pathways, which range in energy-dependent on the transition dipole probability of interband and intraband transitions. (B) After direct $E_{\rm g,opt}$ excitation, no hot carriers are observed, and instead, trion-type exciton formation and relaxation occur through E1, while $V_{\rm O}$ trap recombination is expected for V1 and V2 terms. The range of R1 and R2 (3.65 and 0.80 eV, respectively) are constrained by the detection limits of the instrument.

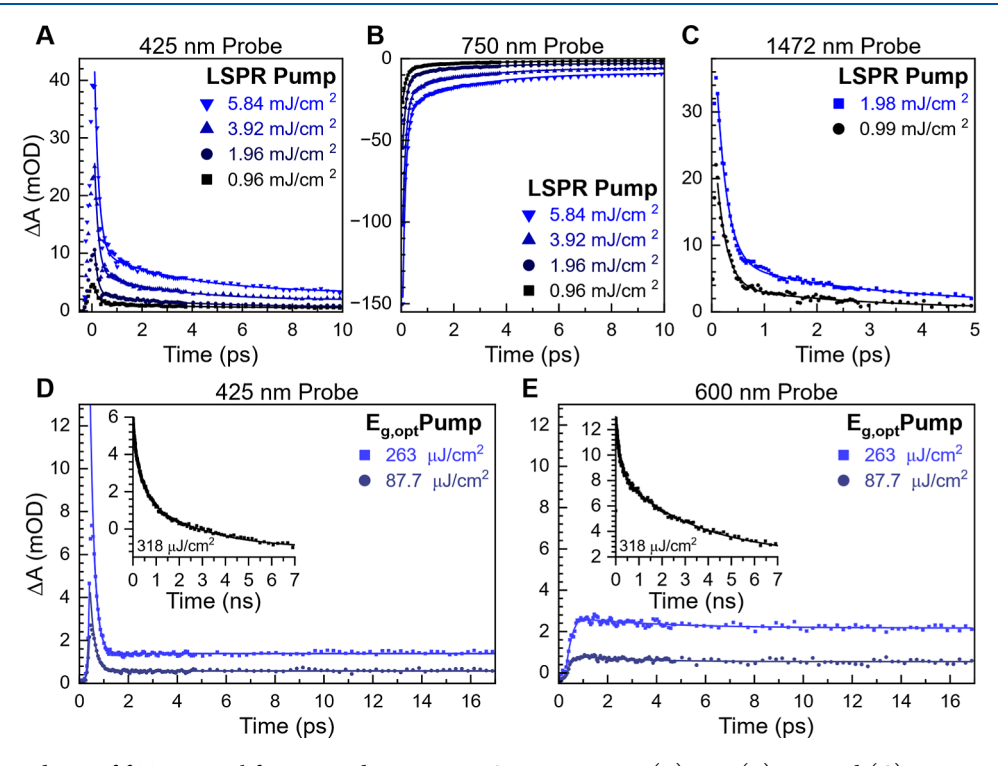


Figure 3. Time dependence of fsTA spectral features under 800 nm, LSPR pumping at (A) 425, (B) 750, and (C) 1472 nm probe wavelengths with biexponential fits. fsTA following excitation of the optical gap at 325 nm, $E_{g,opt}$ is also monitored at (D) 425 and (E) 600 nm probe wavelengths. The transient signal shows drastically different decay dynamics, with long nanosecond time dynamics shown in the insets for both probe wavelengths.

probability of energy transfer from thermalized carriers into the lattice. When holistically comparing R1 and R2 versus B1, the difference in lifetimes suggests that there is a coupling parameter between the band structure and hot carriers as suggested previously;¹⁵ otherwise R1 and R2 lifetimes would be nearly identical to B1.

From the fluence dependence of B1, it is possible to extract the electron–phonon coupling constant, as reported previously for WO_{3-x} . When the LSPR is excited, a rapid transfer of

energy from hot carriers to the lattice occurs due to their difference in electronic temperature, leading to a significant increase in temperature. Such values can be used for further analysis such as the two-temperature model, which takes the differences in temperature into account and provides a way to calculate the thermal response of the material under light excitation. The electron—phonon coupling constant provides a measure of the thermalization behavior, which is important for applications susceptible to thermal damage. ⁴² Following the

work of Johns et al., the electron—phonon coupling constant, *G*, can be calculated using eqs 1 and 2

$$\tau_0 = \frac{\gamma T_0}{G} \tag{1}$$

$$\frac{\gamma_{\text{real},1}}{\gamma_{\text{real},2}} = \frac{m_1 \sqrt[3]{n_{\text{e},1}}}{m_2 \sqrt[3]{n_{\text{e},2}}}$$
(2)

From the fluence dependence for B1 (Figure S9), the parameter τ_0 (el—ph decay rate at zero fluence) is extracted using a linear regression of the three lowest fluences (gray dashed line), assuming a temperature of 298 K for the surroundings of the NC (T_0) and compared with previous literature in Table 2. The results from Johns et al. on WO_{3-x}

Table 2. TTM Parameters Obtained from the Fluence Dependence of B1

	$y (J K^{-2} cm^{-3})$	$G (J K^{-1} s^{-1} cm^{-3})$
B1 (this work)	6.69×10^{-5}	1.47×10^{11}
Johns et al.	5.50×10^{-5}	9.64×10^{10}

are very comparable to this work; the primary difference is likely due to the observation of a lower τ_0 , either due to the lower pulse width capabilities of the fsTA, resulting in a more accurate value, or to the much higher plasmon frequency for this WO_{3-x} sample, resulting in higher carriers and higher el—ph coupling.

In Figure 2B, the TA results are shown for the direct excitation of $E_{\rm g,opt}$ (3.8 eV) at low fluence (263 μ J). Low power prevents ligand dissociation from the NC surface and two-photon effects. In the TA spectra, three distinct absorption features are observed and labeled E1, V1, and V2. The observed dynamics for E1, V1, and V2 are visualized in Figure 3D,E and compiled in Table 3. The long nanosecond lifetimes for V1 and V2 were obtained separately at a power of 318 μ J/cm³ as shown in the inset of Figure 3D,E.

Table 3. $E_{g,opt}$ Pumped (3.8 eV) UV-Vis Probe Lifetimes

$E_{ m g,opt}$ pump feature (energy)	growth $(au_{ ext{growth}}, ext{ fs})$	$_{(\tau_{\text{decay}}, \text{ fs})}^{\text{decay}}$	$_{(\tau_{\text{decay}}, \text{ ns})}^{\text{decay}}$
E1 (2.92 eV)	58.6 ± 1.8	177.5 ± 4.1	
V1 (2.92 eV)			2.68 ± 0.19
V2 (2.07 eV)	273.5 ± 52.8		3.50 ± 0.26

The exciton Auger recombination is assigned as E1 at 3.02 eV nm. The E1 feature decays on the fs time scale commensurate with the appearance of V1 and V2 at 2.92 and 2.19 eV, respectively, which decay on the nanosecond domain. It is difficult to deconvolute E1 and V1 from each other due to energy overlap; however, the rapid growth and decay dynamics can be obtained from E1, while the longtime decay can be obtained for V1 at 2.92, reflecting the longer lifetime for V1. V2 is separately monitored at 2.07 eV for its growth and decay dynamics, with minimal convolution from E1 and V1.

Based on the literature precedence for n-type semiconductor exciton recombination dynamics, 43 E1 is assigned to trion recombination between excitons and free electrons, while V1 and V2 represent the growth of two long-lived acceptor—donor state populations associated with trapping at V_0 sites forming a trapped polaron, analogous to an f-center in oxides. 44 The

energy of the V1 state is consistent with a transition from a V_O^{2+} acceptor level to a V_O^0 donor level, as previously reported. 34 $V_O^{2+} \rightarrow V_O^0$ is a two-electron process, which requires either a $W^{5+}{-}V_O^0{-}W^{5+}$ or $W^{4+}{-}V_O^0{-}W^{6+}$ bonding configuration and is likely to account for the 3.1 eV emission observed. 45 The nanosecond lifetime of V1 and V2 are similar in time scale to the observed power-law behavior in the PL emission in Figure 1B. The V2 state at 2.19 eV is attributed to the V_O^0 donor state to a V_O^+ trap center transition. 46 There is no PL observable for this V_O transition, likely due to Augertype recombination due to the high electron density from the LSPR on resonance with the $V_O^+ \rightarrow V_O^0$ transition energy near the Fermi level. When compared to the LSPR-pumped series (R1, R2, and B1), the E1, V1, and V2 features are clearly distinct and do not display biexponential decay behavior.

CONCLUSIONS

Based on the TA dynamic studies and the proposed scheme for carrier relaxation, $E_{\rm gopt}$ pumped transitions originate from the electronic band structure of WO_{3-x} itself, without interaction of the visible LSPR. Our findings support the idea that the LSPR is a resonance state, which requires direct excitation to access, implying that plasmonic semiconductor oxides can be utilized for their semiconducting properties and plasmonic properties separately or in tandem. Exciting $E_{\rm g,opt}$ directly allows access to the electronic band structure through pathways unique to the semiconductor band structure without hot carrier activation.

Using fsTA, this work thoroughly explores hot carrier dynamics in WO_{2.76} PSNCs as a model system for other n-type plasmonic transparent conducting oxide-type systems. Hot carriers are observed to form only under LSPR pumping and to relax through both interband and intraband pathways. Excitation of the optical band gap leads to trion recombination and emissive pathways due to donor and acceptor level transitions such as Vo's. This study shows that Landau damping-induced carrier formation following LSPR excitation leads to identifiable relaxation processes in WO_{3-x}. Defective tungstate, a plasmonic semiconductor, is observed to have a carrier density approaching noble metals such as gold, and hotcarrier relaxation lifetimes are on similar time scales. The observation of hot carriers in WO_{3-x} suggests that this may be a more economical material for application toward hot-carrier enhancement in integrated devices where gold is normally used to improve device efficiencies.3 This work gleans into the possibility of future PSNCs that could be engineered for dual excitonic/plasmonic-based applications simply by changing the energy of incident photon energy.

ASSOCIATED CONTENT

Supporting Information

The Supporting Information is available free of charge at https://pubs.acs.org/doi/10.1021/acs.jpcc.3c05208.

Decay dynamics of TOPO-WO $_{3-x}$ LSPR in air; HAADF-STEM NC size analysis; pXRD simulations for 2 nm WO $_{3-x}$ compared with experimental pXRD; XPS for WO $_{3-x}$ stoichiometry; Tauc plot analysis of WO $_{3-x}$ optical bandgap; chemical titration of WO $_{3-x}$ LSPR monitored through extinction spectroscopy; additional spectral plots of LSPR-pumped fsTA data; fsTA white light probe spectrum; fluence dependence of

LSPR pumping regimes; and time dependence of fsTA features under LSPR and $E_{g,opt}$ pumping (PDF)

AUTHOR INFORMATION

Corresponding Authors

Richard D. Schaller — Center for Nanoscale Materials, Argonne National Laboratory, 9700 S Cass Ave., Lemont, Illinois 60439, United States; and Department of Chemistry, Northwestern University, Evanston, Illinois 60208, United States; Email: shaller@anl.gov

Geoffrey F. Strouse — Department of Chemistry and Biochemistry, Florida State University, Tallahassee, Florida 32306, United States; orcid.org/0000-0003-0841-282X; Email: strouse@chem.fsu.edu

Authors

Jason E. Kuszynski — Department of Chemistry and Biochemistry, Florida State University, Tallahassee, Florida 32306, United States; Occid.org/0000-0002-9458-6940

Catherine J. Fabiano – Department of Chemistry and Biochemistry, Florida State University, Tallahassee, Florida 32306, United States

Edward T. Nguyen – Department of Chemistry and Biochemistry, Florida State University, Tallahassee, Florida 32306, United States; orcid.org/0000-0002-4787-8270

Keyou Mao − National High Magnetic Field Laboratory, Tallahassee, Florida 32310, United States; Department of Industrial and Manufacturing Engineering, FAMU-FSU College of Engineering, Tallahassee, Florida 32310, United States; orcid.org/0000-0002-2909-8131

Anoushka K. Ahuja – Department of Computer Science, Florida State University, Tallahassee, Florida 32306, United States

Complete contact information is available at: https://pubs.acs.org/10.1021/acs.jpcc.3c05208

Author Contributions

The manuscript was written through the contributions of all authors. All authors have given approval to the final version of the manuscript. J.E.K.: conceptualization, methodology, validation, formal analysis, investigation, data curation, writing—original draft, writing—review and editing, visualization, and project administration. C.J.F.: conceptualization, methodology, validation, formal analysis, investigation, writing—review and editing, and visualization. E.T.N.: validation, formal analysis, and visualization. K.M.: investigation. A.K.A.: investigation. R.D.S.: methodology, validation, investigation, resources, and writing—review and editing. G.F.S.: conceptualization, writing—original draft, writing—review and editing, supervision, project administration, and funding acquisition.

Notes

The authors declare no competing financial interest.

ACKNOWLEDGMENTS

J.E.K., C.J.F., E.T.N., and G.F.S. wish to thank the National Science Foundation (DMR-1905757) "Tuning Plasmonic and Magneto-Plasmonic Behavior in 4-d Transition Metal Doped Indium Oxide" for funding. The project used resources provided by the X-ray Crystallography Center (FSU075000X-RAY) and the Materials Characterization Laboratory (FSU075000MAC) at the FSU Department of Chemistry and Biochemistry. J.E.K. and C.J.F. wish to thank the

Department of Defense for funding from the SMART Scholarship under OUSD/R&E, NDEP/BA-1. Work performed at the CNMs, a U.S. Department of Energy Office of Science User Facility, was supported by the U.S. DOE, Office of Basic Energy Sciences, under contract no. DE-AC02-06CH11357.

REFERENCES

- (1) Polman, A. Plasmonics Applied. Science **2008**, 322 (5903), 868–869.
- (2) Tang, H.; Tang, Z.; Bright, J.; Liu, B.; Wang, X.; Meng, G.; Wu, N.; Wu, N. Visible-Light Localized Surface Plasmon Resonance of WO_{3-x} Nanosheets and Its Photocatalysis Driven by Plasmonic Hot Carriers. ACS Sustain. Chem. Eng. 2021, 9 (4), 1500–1506.
- (3) Hattori, Y.; Gutiérrez Álvarez, S.; Meng, J.; Zheng, K.; Sá, J. Role of the Metal Oxide Electron Acceptor on Gold-Plasmon Hot-Carrier Dynamics and Its Implication to Photocatalysis and Photovoltaics. *ACS Appl. Nano Mater.* **2021**, *4* (2), 2052–2060.
- (4) Agrawal, A.; Johns, R. W.; Milliron, D. J. Control of Localized Surface Plasmon Resonances in Metal Oxide NCs. *Annu. Rev. Mater. Res.* **2017**, *47* (1), 1–31.
- (5) Agrawal, A.; Cho, S. H.; Zandi, O.; Ghosh, S.; Johns, R. W.; Milliron, D. J. Localized Surface Plasmon Resonance in Semi-conductor NCs. *Chem. Rev.* **2018**, *118* (6), 3121–3207.
- (6) Liu, Z.; Zhong, Y.; Shafei, I.; Borman, R.; Jeong, S.; Chen, J.; Losovyj, Y.; Gao, X.; Li, N.; Du, Y.; et al. Tuning Infrared Plasmon Resonances in Doped Metal-Oxide NCs through Cation-Exchange Reactions. *Nat. Commun.* **2019**, *10* (1), 1394.
- (7) Ghorai, N.; Ghosh, H. N. Ultrafast Plasmon Dynamics and Hole-Phonon Coupling in NIR Active Nonstoichiometric Semiconductor Plasmonic Cu _{2-x} S NCs. *J. Phys. Chem. C* **2019**, *123* (46), 28401–28410.
- (8) Zhou, D.; Li, X.; Zhou, Q.; Zhu, H.; Qiaohui, Z.; Qiaohui, Z.; Zhu, H.; Haiming, Z. Infrared driven hot electron generation and transfer from non-noble metal plasmonic NCs. *Nat. Commun.* **2020**, *11* (1), 2944.
- (9) Yin, H.; Kuwahara, Y.; Mori, K.; Louis, C.; Yamashita, H. Properties, Fabrication and Applications of Plasmonic Semiconductor NCs. *Catal. Sci. Technol.* **2020**, *10* (13), 4141–4163.
- (10) Cong, S.; Geng, F.; Zhao, Z. Tungsten Oxide Materials for Optoelectronic Applications. *Adv. Mater.* **2016**, 28 (47), 10518–10528.
- (11) Manthiram, K.; Alivisatos, A. P. Tunable Localized Surface Plasmon Resonances in Tungsten Oxide NCs. *J. Am. Chem. Soc.* **2012**, 134 (9), 3995–3998.
- (12) Prusty, G.; Lee, J. T.; Seifert, S.; Muhoberac, B. B.; Sardar, R.; Sardar, R. Ultrathin Plasmonic Tungsten Oxide Quantum Wells with Controllable Free Carrier Densities. *J. Am. Chem. Soc.* **2020**, *142* (13), 5938–5942.
- (13) Salje, E.; Güttler, B. Anderson Transition and Intermediate Polaron Formation in WO_{3-x} Transport Properties and Optical Absorption. *Phil. Mag. B* **1984**, *50* (5), 607–620.
- (14) Schirmer, O. F.; Salje, E. Conduction Bipolarons in Low-Temperature Crystalline WO_{3-x}. *J. Phys. C: Solid State Phys.* **1980**, *13* (36), L1067–L1072.
- (15) Kenny-Wilby, A.; Jaics, G.; Zhang, C.; Yin, P.; Radovanovic, P. V. Revisiting Plasmonic Properties of Complex Semiconductor NCs Using Magnetic Circular Dichroism Spectroscopy: A Cautionary Tale. *J. Phys. Chem. C* **2023**, *127* (2), 1087–1096.
- (16) Villegas, C. E. P.; Leite, M. S.; Marini, A.; Rocha, A. R. Efficient Hot-Carrier Dynamics in near-Infrared Photocatalytic Metals. *Phys. Rev. B* **2022**, *105* (16), 165109.
- (17) Liu, Q.; Wu, Y.; Zhang, J.; Chen, K.; Huang, C.; Chen, H.; Qiu, X. Plasmonic MoO_{3-x} Nanosheets with Tunable Oxygen Vacancies as Efficient Visible Light Responsive Photocatalyst. *Appl. Surf. Sci.* **2019**, 490, 395–402.

- (18) Li, X.; Xiao, D.; Zhang, Z.; Zhenyu, Z. Landau Damping of Quantum Plasmons in Metal Nanostructures. *New J. Phys.* **2013**, *15* (2), 023011.
- (19) Conti III, C. R.; Quiroz-Delfi, G.; Schwarck, J. S.; Chen, B.; Strouse, G. F. Carrier Density, Effective Mass, and Nuclear Relaxation Pathways in Plasmonic Sn:In2O3 NCs. *J. Phys. Chem. C* **2020**, 124 (51), 28220–28229.
- (20) Kays, J. C.; Conti, C. R.; Margaronis, A.; Kuszynski, J. E.; Strouse, G. F.; Dennis, A. M. Controlled Synthesis and Exploration of Cu_xFeS₄ Bornite NCs. *Chem. Mater.* **2021**, 33 (18), 7408–7416.
- (21) Gibbs, S. L.; Staller, C. M.; Agrawal, A.; Johns, R. W.; Saez Cabezas, C. A.; Milliron, D. J. Intrinsic Optical and Electronic Properties from Quantitative Analysis of Plasmonic Semiconductor NC Ensemble Optical Extinction. *J. Phys. Chem. C* **2020**, *124* (44), 24351–24360.
- (22) White, T. P.; Catchpole, K. R. Plasmon-Enhanced Internal Photoemission for Photovoltaics: Theoretical Efficiency Limits. *Appl. Phys. Lett.* **2012**, *101* (7), 073905.
- (23) Jang, Y. H.; Jang, Y. J.; Kim, S.; Quan, L. N.; Chung, K.; Kim, D. H. Plasmonic Solar Cells: From Rational Design to Mechanism Overview. *Chem. Rev.* **2016**, *116* (24), 14982–15034.
- (24) Christopher, P.; Moskovits, M. Hot Charge Carrier Transmission from Plasmonic Nanostructures. *Annu. Rev. Phys. Chem.* **2017**, 68 (1), 379–398.
- (25) Amendola, V.; Pilot, R.; Frasconi, M.; Maragò, O. M.; Iati, M. A. Surface Plasmon Resonance in Gold Nanoparticles: A Review. *J. Phys.: Condens. Matter* **2017**, 29 (20), 203002.
- (26) Tang, H.; Chen, C.-J.; Huang, Z.; Bright, J.; Meng, G.; Liu, R. S.; Wu, N.; Wu, N. Plasmonic Hot Electrons for Sensing, Photodetection, and Solar Energy Applications: A Perspective. *J. Chem. Phys.* **2020**, *152* (22), 220901.
- (27) Shen, Y.; Roberge, A.; Tan, R.; Gee, M. Y.; Gary, D. C.; Huang, Y.; Blom, D. A.; Benicewicz, B. C.; Cossairt, B. M.; Greytak, A. B. Gel Permeation Chromatography as a Multifunctional Processor for NC Purification and On-Column Ligand Exchange Chemistry. *Chem. Sci.* **2016**, 7 (9), 5671–5679.
- (28) Washington Ii, A. L.; Strouse, G. F. Microwave Synthesis of CdSe and CdTe NCs in Nonabsorbing Alkanes. *J. Am. Chem. Soc.* **2008**, *130* (28), 8916–8922.
- (29) Shubert-Zuleta, S. A.; Tandon, B.; Roman, B. J.; Gan, X. Y.; Milliron, D. J. How to Quantify Electrons in Plasmonic Colloidal Metal Oxide NCs. *Chem. Mater.* **2023**, *35*, 3880–3891.
- (30) Conti, C. R.; McBride, J. R.; Strouse, G. F. Examining the Effect of Dopant Ionic Radius on Plasmonic M:ZnO NCs (M = Al3+, Ga3+, In3+). *J. Phys. Chem. C* **2021**, 125 (14), 7772–7779.
- (31) Luo, J. Y.; Xu, N. S.; Zhao, F. L.; Deng, S. Z.; Tao, Y. T. Ultraviolet Superfluorescence from Oxygen Vacancies in WO3-x Nanowires at Room Temperature. *J. Appl. Phys.* **2011**, *109* (2), 024312.
- (32) Johansson, M. B.; Zietz, B.; Niklasson, G. A.; Österlund, L. Optical Properties of NCline WO 3 and WO 3-x Thin Films Prepared by DC Magnetron Sputtering. *J. Appl. Phys.* **2014**, *115* (21), 213510.
- (33) Wang, B. B.; Zhong, X. X.; He, C. L.; Zhang, B.; Shao, R. W.; Shvalya, V.; Cvelbar, U.; Ostrikov, K. Controlling Oxygen Vacancies of WO Suboxides by ZnWO4 Nanophase Hybridization. *Mater. Sci. Eng. B* **2020**, 262, 114706.
- (34) Wang, B. B.; Zhong, X.; He, C.; Zhang, B.; Cvelbar, U.; Ostrikov, K.; Zhang, B.-J.; Cvelbar, U.; Cvelbar, U.; Ostrikov, K. Nanostructure Conversion and Enhanced Photoluminescence of Vacancy Engineered Substoichiometric Tungsten Oxide Nanomaterials. *Mater. Chem. Phys.* **2021**, *262*, 124311.
- (35) Camarda, P.; Messina, F.; Vaccaro, L.; Agnello, S.; Buscarino, G.; Schneider, R.; Popescu, R.; Gerthsen, D.; Lorenzi, R.; Gelardi, F. M.; Cannas, M. Luminescence Mechanisms of Defective ZnO Nanoparticles. *Phys. Chem. Chem. Phys.* **2016**, *18* (24), 16237–16244. (36) Galland, C.; Ghosh, Y.; Steinbrück, A.; Hollingsworth, J. A.; Htoon, H.; Klimov, V. I. Lifetime Blinking in Nonblinking NC Quantum Dots. *Nat. Commun.* **2012**, *3* (1), 908.

- (37) Brongersma, M. L.; Halas, N. J.; Nordlander, P. Plasmon-Induced Hot Carrier Science and Technology. *Nat. Nanotechnol.* **2015**, *10* (1), 25–34.
- (38) Hodak, J.; Martini, I.; Hartland, G. V. Ultrafast Study of Electron-Phonon Coupling in Colloidal Gold Particles. *Chem. Phys. Lett.* **1998**, 284 (1–2), 135–141.
- (39) González-Borrero, P. P.; Sato, F.; Medina, A. N.; Baesso, M. L.; Bento, A. C.; Baldissera, G.; Persson, C.; Niklasson, G. A.; Granqvist, C. G.; Ferreira Da Silva, A. Optical Band-Gap Determination of Nanostructured WO3 Film. *Appl. Phys. Lett.* **2010**, *96* (6), 061909.
- (40) Link, S.; El-Sayed, M. A. Spectral Properties and Relaxation Dynamics of Surface Plasmon Electronic Oscillations in Gold and Silver Nanodots and Nanorods. *J. Phys. Chem. B* **1999**, *103* (40), 8410–8426.
- (41) Johns, R. W.; Blemker, M. A.; Azzaro, M. S.; Heo, S.; Runnerstrom, E. L.; Milliron, D. J.; Roberts, S. T. Charge Carrier Concentration Dependence of Ultrafast Plasmonic Relaxation in Conducting Metal Oxide NCs. *J. Mater. Chem. C* **2017**, *5* (23), 5757–5763.
- (42) Khosravi Khorashad, L.; Argyropoulos, C. Unraveling the Temperature Dynamics and Hot Electron Generation in Tunable Gap-Plasmon Metasurface Absorbers. *Nanophotonics* **2022**, *11* (17), 4037–4052.
- (43) Klochikhin, A. A.; Kochereshko, V. P.; Besombes, L.; Karczewski, G.; Wojtowicz, T.; Kossut, J. Plasmon Mechanism of the Trion Emission Band Broadening in Quantum Wells. *Phys. Rev. B: Condens. Matter Mater. Phys.* **2011**, 83 (23), 235329.
- (44) Arora, H. L.; Wang, S. Application of the Polaron Model to the F' Center. *J. Phys. Chem. Solids* **1969**, *30* (7), 1649–1660.
- (45) Deb, S. K. Opportunities and Challenges in Science and Technology of WO3 for Electrochromic and Related Applications. *Sol. Energy Mater. Sol. Cells* **2008**, *92* (2), 245–258.
- (46) Wang, F.; Pacchioni, G.; Di Valentin, C.; Pacchioni, G. Semiconductor-to-Metal Transition in WO 3 X: Nature of the Oxygen Vacancy. *Phys. Rev. B: Condens. Matter Mater. Phys.* **2011**, 84 (7), 073103.